PROCEEDINGS OF SCIENCE

ONLINE ICRC 2021
THE ASTROPARTICLE PHYSICS CONFERENCE
Berlin | Germany
37th International Cosmic Ray Conference
12–23 July 2021

A Peculiar ICME Event in August 2018 Observed with the Global Muon Detector Network

Kazuoki Munakata[a,*] **on behalf of the GMDN Collaboration**
(a complete list of authors can be found at the end of the proceedings)

[a] *Physics Department, Shinshu University,*
3-1-1 Asahi, Matsumoto, Nagano 390-8621, Japan
E-mail: kmuna00@shinshu-u.ac.jp

We demonstrate that global observations of high-energy cosmic rays contribute to understanding unique characteristics of a large-scale magnetic flux rope (MFR) causing a magnetic storm in August 2018. Following a weak interplanetary shock on 25 August 2018, a MFR caused an unexpectedly large geomagnetic storm. It is likely that this event became geoeffective because the MFR was accompanied by a corotating interaction region (CIR) and compressed by high-speed solar wind following the MFR. In fact, a Forbush decrease was observed in cosmic-ray data inside the MFR as expected, and a significant cosmic-ray density increase exceeding the unmodulated level before the shock was also observed near the trailing edge of the MFR. The cosmic-ray density increase can be interpreted in terms of the adiabatic heating of cosmic rays near the trailing edge of the MFR, as the corotating interaction region prevents free expansion of the MFR and results in the compression near the trailing edge. A northeast-directed spatial gradient in the cosmic-ray density was also derived during the cosmic-ray density increase, suggesting that the center of the heating near the trailing edge is located northeast of Earth. The second order anisotropy is observed during the density increase clearly representing an intensity enhancement of cosmic rays with approximately 90 degree pitch angle, possibly indicating the betatron acceleration of CRs during the cosmic-ray density increase and/or accelerated CRs leaking along the magnetic field from the density increase region toward the south where lower CR population is expected. This is one of the best examples demonstrating that the observation of high energy cosmic rays provides us with information of the three-dimensional macroscopic picture of the interaction between coronal mass ejections and the ambient solar wind, which is essential for prediction of large magnetic storms.

37th International Cosmic Ray Conference (ICRC 2021)
July 12th – 23rd, 2021
Online – Berlin, Germany

*Presenter

© Copyright owned by the author(s) under the terms of the Creative Commons
Attribution-NonCommercial-NoDerivatives 4.0 International License (CC BY-NC-ND 4.0).

PoS(ICRC2021)1265

1. Event overview

Figure 1 summarizes solar wind parameters measured in an ICME over four days between 24 and 27 August, 2018 (https://omniweb.gsfc.nasa.gov/ow.html). This ICME event is caused by a CME eruption recorded at 21:24 UT on 20 August by the LASCO coronagraphs on board the *SOHO* satellite. Following a weak IP-shock recorded at 03:00 UT on 25 August (see the pink vertical line in Figure 1) and a successive sheath period identified by the enhanced fluctuation of IMF (a period between the pink and the first blue lines), a significant enhancement of the IMF magnitude is recorded until 09:09 UT on 26 August in association with a systematic rotation of IMF orientation indicating Earth's entrance into the MFR. Following *Chen et al.* [1], we define the MFR period as a period between 14:10 UT on 25 August and 09:09 UT on 26 August, delimited by a pair of blue vertical lines. A significant southward field is recorded in the MFR causing a gradual decrease of the D_{ST} index of geomagnetic field down to the minimum of -174 nT at 06:00 on 26 August (panel e)(http://wdc.kugi.kyoto-u.ac.jp/index.html). Following the MFR period, the gradual increase of solar wind speed is recorded.

This event occurred in 2018 close to the solar activity minimum of solar cycle 24. The CME was relatively slow taking about five days to arrive at Earth after the CME eruption on the Sun. The solar wind velocity enhancement after the IP-shock is also weak and seems to be insufficient to cause the large solar wind compression and significant enhancement of the southward IMF that triggered a major geomagnetic storm. *Chen et al.* [1] attributed peculiarities of this storm to the MFR compression by the following faster solar wind and *Dal Lago et al.* [3] also presented a similar idea of MFR compression for an event that occurred in October 1999. In this paper, we study this peculiar ICME event by analyzing the cosmic-ray data from the Global Muon Detector Network (GMDN). For more detail of our analysis, readers can refer to our recent paper *Kihara et al.* [4]. *Abunin et al.* [2] reported a strong enhancement of the cosmic-ray (CR) anisotropy during this event from the observations with neutron monitors.

2. Analysis of GMDN data

The GMDN, which is designed for accurate observation of the GCR anisotropy, comprises four multidirectional muon detectors recording muon count rates in 60 directional channels viewing almost the entire sky around Earth. The median rigidity (P_m) of primary GCRs recorded by the GMDN, which we calculate by using the response function of the atmospheric muons to the primary GCRs given by numerical solutions of the hadronic cascade in the atmosphere [5], ranges from about 50 GV for the vertical directional channel to about 100 GV for the most inclined directional channel, while the asymptotic viewing directions (corrected for geomagnetic bending of cosmic-ray orbits) at P_m covers the asymptotic viewing latitude (λ_{asymp}) from 72°N to 77°S. The representative P_m of the entire GMDN is about 60 GV. More detail information of the GMDN can be found in our separate paper [6].

We analyze the percent deviation of the 10-minute muon count rate $I_{i,j}(t)$ from an average over 27 days between 12 August and 7 September, 2018 in the j-th directional channel of the i-th detector in the GMDN at universal time t, after correcting for local atmospheric pressure and temperature

PoS(ICRC2021)1265

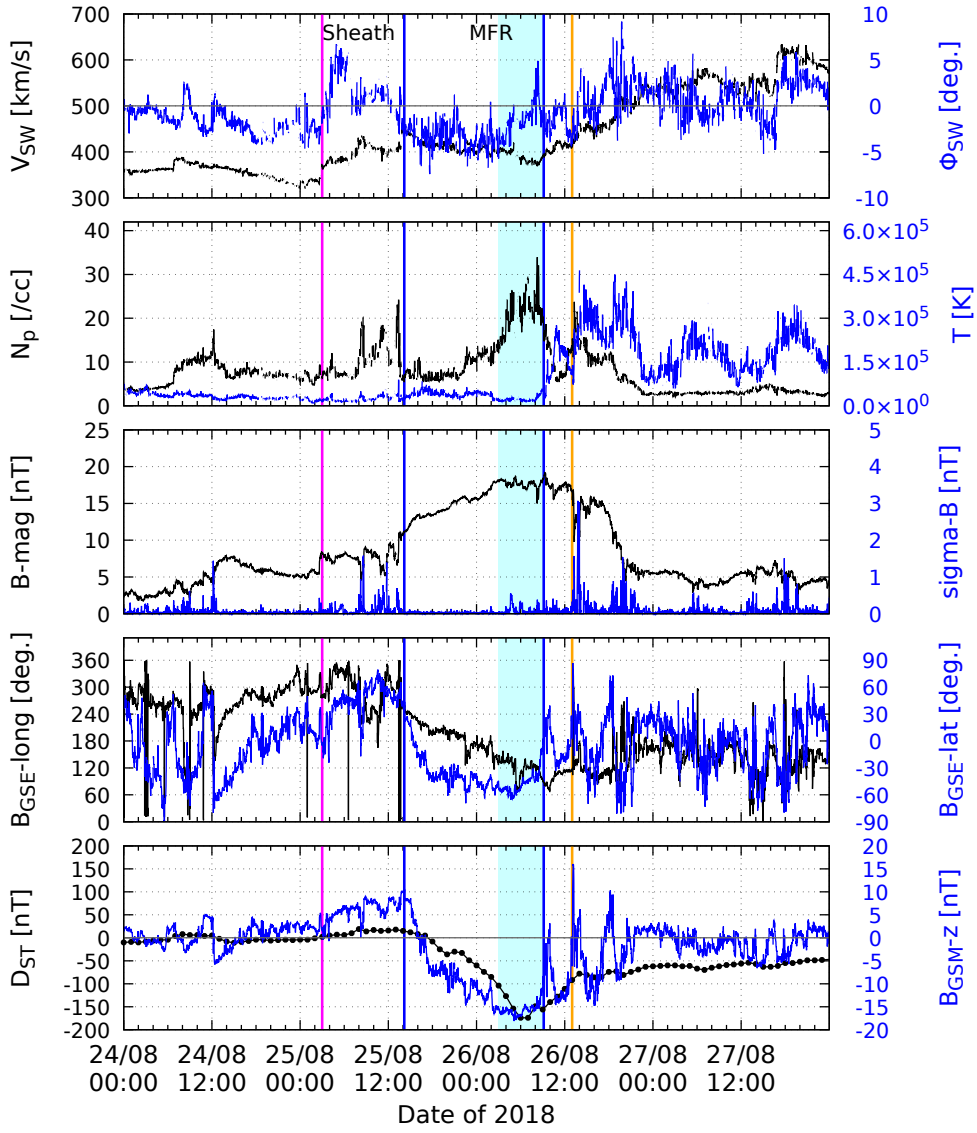

Figure 1: Solar wind parameters and D_{ST} index for 24-27 August, 2018. The pink vertical line indicates the timing of IP-shock identified by the shock of IMF at 03:00 UT on 25 August, while a pair of blue vertical lines delimit the MFR period reported by *Chen et al.* [1]. The blue shaded area indicates six hours between 03:00 UT and 09:00 UT on 26 August when an increase is observed in the cosmic-ray density (see text). The orange vertical line indicates the second stream interface at 13:00 UT on 26 August. As indicated at the top of the figure, we define the "MFR period" delimited by a pair of blue vertical lines and the "sheath period" between the pink and the first blue vertical lines (see text).

PoS(ICRC2021)1265

effects. For our correction method of the atmospheric effects using the on-site measurement of pressure and the mass weighted temperature from the vertical profile of the atmospheric temperature provided by the Global Data Assimilation System (GDAS) of the National Center for Environmental Prediction, readers can refer to *Mendonça et al.* [7].

We model $I_{i,j}(t)$ in terms of the cosmic ray density (or omnidirectional intensity) $I_0(t)$ and three components of the first order anisotropy ($\xi_x^{\rm GEO}(t), \xi_y^{\rm GEO}(t), \xi_z^{\rm GEO}(t)$) of $\boldsymbol{\xi}(t)$ in a geocentric (GEO) coordinate system, as

$$\begin{aligned} I_{i,j}^{fit}(t) = I_0(t)c_{0\ i,j}^0 \ + \ \xi_x^{\rm GEO}(t)f_{1\ i,j}^1(t_i) \ + \ \xi_y^{\rm GEO}(t)g_{1\ i,j}^1(t_i) \ + \ \xi_z^{\rm GEO}(t)c_{1\ i,j}^0 \\ + \ \xi_2^{0\ \rm GEO}(t)c_{2\ i,j}^0 + \ \ \xi_2^{1c\ \rm GEO}(t)f_{2\ i,j}^1(t_i) \ + \ \xi_2^{1s\ \rm GEO}(t)g_{2\ i,j}^1(t_i) \\ + \ \xi_2^{2c\ \rm GEO}(t)f_{2\ i,j}^2(t_i) \ + \ \xi_2^{2s\ \rm GEO}(t)g_{2\ i,j}^2(t_i), \end{aligned} \tag{1}$$

where

$$\begin{aligned} f_{n\ i,j}^m(t_i) &= c_{n\ i,j}^m \cos m\omega t_i - s_{n\ i,j}^m \sin m\omega t_i, \\ g_{n\ i,j}^m(t_i) &= s_{n\ i,j}^m \cos m\omega t_i + c_{n\ i,j}^m \sin m\omega t_i, \end{aligned} \tag{2}$$

t_i is the local time in hours at the i-th detector, $\omega = \pi/12$, and $c_{m\ i,j}^n$ and $s_{m\ i,j}^n$ are the coupling coefficients which relate (or "couple") the observed intensity in each directional channel with the cosmic ray density and anisotropy in space. In the GEO coordinate system, we set the x-axis to the anti-sunward direction in the equatorial plane, the z-axis to the geographical north perpendicular to the equatorial plane and the y-axis completing the right-handed coordinate system. Coupling coefficients in Eq.(2) are calculated by using the response function of the atmospheric muon intensity to primary GCRs [5] and by assuming $I_0(t)$ inversely proportional to the rigidity P of primary CRs and the (first- and second-order) anisotropies independent of P. We derive the best-fit set of nine parameters ($I_0(t)$, $\xi_x^{\rm GEO}(t)$, $\xi_y^{\rm GEO}(t)$, $\xi_z^{\rm GEO}(t)$ and $\xi_2^{m\ c/s\ \rm GEO}(t)$ with $0 \leqq m \leqq 2$) minimizing the residual value of fitting defined, as

$$\chi^2 = \sum_{i,j} (I_{i,j}(t) - I_{i,j}^{fit}(t))^2 / \sigma_{c\ i,j}^2 \tag{3}$$

with $\sigma_{ci,j}$ denoting the count rate error of $I_{i,j}(t)$. The best-fit anisotropy vector $\boldsymbol{\xi}^{\rm GEO}(t)$ in the GEO coordinate system is then transformed to $\boldsymbol{\xi}^{\rm GSE}(t)$ in the geocentric solar ecliptic (GSE) coordinate system for comparisons with the solar wind and IMF data.

We first subtract from $\boldsymbol{\xi}^{\rm GSE}(t)$ contributions from the solar wind convection and the Compton-Getting effect arising from Earth's revolution around the Sun. In the picture of diffusive propagation of GCRs in the heliosphere, the spatial gradient vector ($\mathbf{G}$) of GCR density is related to the first-order anisotropy, as

$$G(t) = \frac{1}{R_L(t)\alpha_\parallel}\xi_\parallel^w(t) + \frac{\alpha_\perp}{R_L(t)(1+\alpha_\perp^2)}\xi_\perp^w(t) + \frac{1}{R_L(t)(1+\alpha_\perp^2)}\frac{B(t)}{B(t)} \times \xi_\perp^w(t) \tag{4}$$

where $R_L(t) = \frac{P}{c|B(t)|}$ is the Larmor radius of particles with rigidity P in magnetic field $B(t)$ and $\xi_\parallel^w(t)$ and $\xi_\perp^w(t)$ are components of the first-order anisotropy vector parallel and perpendicular

PoS(ICRC2021)1265

to $\mathbf{B}(t)$, respectively [8]. $\alpha_{\parallel}$ and $\alpha_{\perp}$ in Eq.(4) are mean-free-paths of parallel and perpendicular diffusions, respectively, normalized by $R_L(t)$, as

$$\alpha_{\parallel} = \lambda_{\parallel}(t)/R_L(t) \tag{5}$$

$$\alpha_{\perp} = \lambda_{\perp}(t)/R_L(t). \tag{6}$$

According to current understanding that GCRs at neutron monitor and muon detector energies are in the "weak-scattering" regime [9], we assume in this paper $\lambda_{\perp}(t) \ll \lambda_{\parallel}(t)$ and constant $\alpha_{\perp} = 0.36$ for a period outside the MFR, as often used in the study of the large-scale GCR transport in the heliosphere. We also assume $\lambda_{\parallel} = 1.9$ AU for the entire period. For 60 GV cosmic rays in $|\mathbf{B}(t)| \sim 5$ nT average magnetic field, R_L is 0.27 AU resulting in $\lambda_{\perp} = 0.096$ AU and $\alpha_{\parallel} = 7.2$. For a period inside the MFR where the magnetic field is exceptionally strong, we use a constant $\lambda_{\perp} = 0.010$ AU without changing $\lambda_{\parallel}$ [10].

3. Results

3.1 GCR density and density gradient

Figure 2 shows the GCR density ($I_0(t)$) and density gradient ($\mathbf{G}(t)$ at 60 GV obtained from our analyses of the GMDN data. In this paper, we use only the hourly average of six 10-minute values, because one hour is much shorter than the time scale ($R_L/V_{SW} \sim 9$ hours) for the solar wind to travel across the Larmor radius (R_L=0.089 AU) of 60 GV GCRs in IMF ($B \sim 15$ nT) with the average velocity ($V_{SW} \sim 400$ km/s) and enough for analyzing the spatial distribution of 60 GV GCRs. We also calculated the error of the hourly value of each parameter from the dispersion of 10-minute values.

The cosmic-ray density $I_0(t)$ in the top panel starts decreasing a few hours before the IP-shock early on 25 August and goes to the minimum of -0.28 % at 16:30 UT and recovers to the level before the IP-shock early on 26 August. This is a well-known feature of a moderate Forbush decrease indicating Earth's entrance into the cosmic-ray depleted region formed behind the shock and in the magnetic flux rope (MFR). A small local maximum is seen in $I_0(t)$ at around 10:00 UT of 25 August being superposed on the gradual decrease in the sheath period. We think that this is probably due to the discontinuity recorded in the IMF magnitude and longitude seen in Figure 1, because such a local increase of $I_0(t)$ is often observed by the GMDN at the IMF discontinuity [11].

It is seen in the bottom three panels that $G_x(t)$ and $G_y(t)$ change their signs from negative to positive around the time of the minimum $I_0(t)$ in the MFR period, while $G_z(t)$ remains negative. This is qualitatively consistent with the MFR orientation (the elevation angle of the MFR is about $-51°$ and the azimuthal angle is about 299°) presented in *Chen et al.* [1], indicating that the cosmic-ray density minimum region formed along the MFR axis passed northeast of Earth approaching from the sunward direction and then leaving.

A marked feature of this event is a "hump" in the density in which $I_0(t)$ increased to the maximum at around 06:00 UT on 26 August exceeding the unmodulated level before the shock. As discussed in *Kihara et al.* [4], this increase accompanied by a linear decrease of $G_x(t)$ is likely caused by the compression of the trailing edge of the MFR by the faster solar wind following the MFR (see the

PoS(ICRC2021)1265

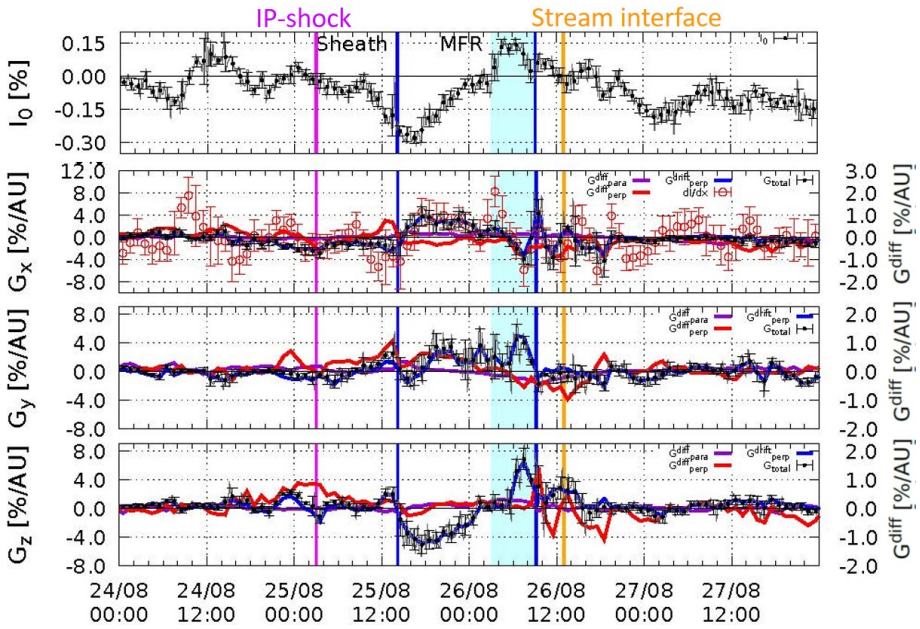

Figure 2: Cosmic-ray density, anisotropy and density gradient at 60 GV derived from GMDN data. Top panel displays cosmic-ray density $I_0(t)$, while bottom panels display three components of $\mathbf{G}(t)$ calculated by Equation (2). In each of bottom three panels, the contribution from the drift is shown by the blue curve on the left vertical axis together with the total gradient component (black solid circles), while contributions from the parallel and perpendicular diffusions are shown by purple and red curves on the right vertical axis, respectively (note the scale of the right vertical axis is expanded four times the left axis). Open red circles in the second panel show $\frac{1}{V_{SW}}\frac{dI_0(t)}{dt}$ calculated with V_{SW} = 400 km/s for a test of $\mathbf{G}(t)$ derived from $\boldsymbol{\xi}^w(t)$.

blue shaded period in Figures 1 and 2). It is interesting to note that the hump is observed in the center of MFR which is significantly shifted toward the trailing edge of the MFR as indicated by the Grad-Shafranov plot by *Chen et al.* [1].

Another notable features of $\mathbf{G}(t)$ are positive enhancements of $G_z(t)$ and $G_y(t)$ in the later MFR period between 03:00 UT and 09:00 UT on 26 August (blue shaded period in Figures 1 and 2) when the orientation of the strongest IMF turned northeast after the maximum of $I_0(t)$ observed in the hump in the top panel. This indicates that a region with higher $I_0(t)$ exists northeast of Earth ($y_{GSE} > 0$, $z_{GSE} > 0$) and a significant diffusion anisotropy from there is observed along the IMF.

3.2 Second-order anisotropy

Top panel of Figure 3 displays the amplitudes of the first-order (blue curve) and second-order (red-curve) anisotropies. It is clear that the amplitude of the second-order anisotropy increases and dominates the first-order anisotropy during the blue-shaded period when the hump of $I_0(t)$ is observed. It is also seen in the bottom panel showing five components of the second-order anisotropy that negative $\xi_2^{0\ \mathrm{GEO}}(t)$ dominates other components during the blue-shaded period. This is consistent with the intensity enhancement of particles with 90° pitch angle measured from $\mathbf{B}(t)$, because $\mathbf{B}(t)$ during this period directs approximately parallel to Earth's spin axis (z_{GEO}).

PoS(ICRC2021)1265

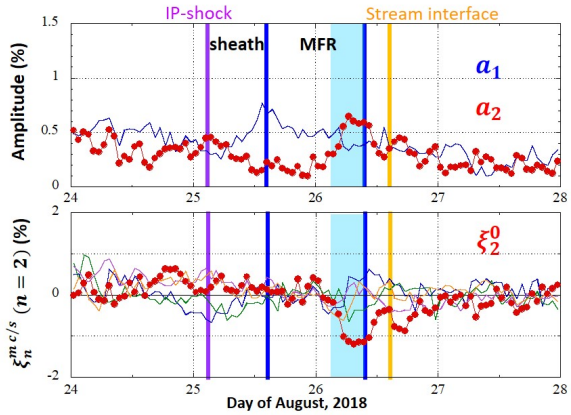

Figure 3: Second-order anisotropy at 60 GV derived from GMDN data for 24-27 August, 2018. Red circles in the upper panel show the amplitude of the second-order anisotropy ($a_2 = \sqrt{((\xi_2^{0\ \mathrm{GEO}})^2 + (\xi_2^{1c\ \mathrm{GEO}})^2 + (\xi_2^{1s\ \mathrm{GEO}})^2 + (\xi_2^{2c\ \mathrm{GEO}})^2 + (\xi_2^{2s\ \mathrm{GEO}})^2)/5}$), while the blue curve shows the amplitude of the first-order anisotropy ($a_1 = \sqrt{((\xi_1^{0\ \mathrm{GEO}})^2 + (\xi_1^{1c\ \mathrm{GEO}})^2 + (\xi_1^{1s\ \mathrm{GEO}})^2)/3}$) for comparison. Red circles in the lower panel show $\xi_2^{0\ \mathrm{GEO}}$, while other color curves display remaining four components of the second-order anisotropy.

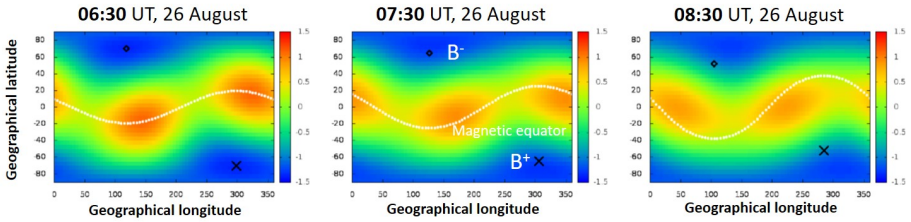

Figure 4: Sample color maps of the hourly mean intensity represented by the best-fit second-order anisotropy during the blue shaded period. Black cross and diamond in each panel represent the orientations parallel and anti-parallel to $\mathbf{B}(t)$, respectively, while the white doted-curve shows the magnetic equator perpendicular to $\mathbf{B}(t)$.

This is actually seen in Figure 4 also showing the intensity enhancement around the magnetic equator. The observed second-order anisotropy possibly suggests the betatron acceleration in the compressed magnetic field (a candidate physical mechanism of the adiabatic heating) in the blue shaded period near the trailing edge of the MFR as well as CRs leaking along $\mathbf{B}(t)$ toward the southwest where the CR population is lower.

4. Conclusions

The observation that, near the trailing edge of the MFR, I_0 rose above its undisturbed level suggests that GCRs gained energy relative to the quiet period. A plausible cause of the energy gain may be a compression of the plasma occurring in the MFR [4]. Positive enhancements of $G_z(t)$ and $G_y(t)$ are observed during the same period when the orientation of the strongest IMF turned

PoS(ICRC2021)1265

northeast after the maximum of $I_0(t)$. This indicates that the center of region with higher $I_0(t)$ exists northeast of Earth ($y_{GSE} > 0$, $z_{GSE} > 0$) and a significant first-order diffusion anisotropy from there is observed along the IMF. In the same period, the amplitude of the second-order anisotropy also increases, possibly suggesting the betatron acceleration in the magnetic field getting compressed as well as CRs leaking along $\mathbf{B}(t)$ toward the southwest where the CR population is lower.

5. Acknowledgement

This work is supported in part by the joint research programs of the National Institute of Polar Research, in Japan, the Institute for Space-Earth Environmental Research (ISEE), Nagoya University, and the Institute for Cosmic Ray Research (ICRR), University of Tokyo. The observations are supported by Nagoya University with the Nagoya muon detector, by INPE and UFSM with the São Martinho da Serra muon detector, by the Australian Antarctic Division with the Hobart muon detector, and by project SP01/09 of the Research Administration of Kuwait University with the Kuwait City muon detector. Global Muon Detector Network data are available at the website (http://cosray.shinshu-u.ac.jp/crest/DB/Public/main.php) of the Cosmic Ray Experimental Science Team (CREST) of Shinshu University. The authors gratefully acknowledge the NOAA Air Resources Laboratory (ARL) for the provision of GDAS data, which are available at READY website (http://www.ready.noaa.gov) and used in this paper. The *Wind* spacecraft data were obtained via the NASA homepage and the hourly D_{ST} index is provided by the WDC for Geomagnetism, Kyoto, Japan.

References

[1] C. Chen *et al.*, *Astrophys. J.*, **884**, 90 (2019)

[2] A. A. Abunin *et al.*, *Solar Phys.*, **295** (2020)

[3] Dal Lago *et al.*, *J. Geophys. Res.*, **111**, A07S14 (2006)

[4] W. Kihara *et al.*, *Space Weather*, **19**, 3 (2021)

[5] K. Murakami *et al.*, *IL NUOVO CIM.*, **2C**, 635 (1979)

[6] Y. Okazaki *et al.*, *Astrophys. J.*, **681**, 693 (2008)

[7] R. R. S. Mendonça *et al.*, *J. Geophys. Res.*, **124** (2019)

[8] M. Kozai *et al.*, *Astrophys. J., 825*, 100 (2016)

[9] J. W. Bieber *et al.*, *Geophys. Res. Lett*, **31** (2004)

[10] K. Munakata *et al.*, *Advances in Geosciences, 21*, **115** (2006)

[11] K. Munakata *et al.*, *Astrophys. J.*, **862**, 170 (2018)

PoS(ICRC2021)1265

Full Authors List: GMDN collaboration

C. Kato[1], K. Munakata[1], W. Kihara[1], R. Kataoka[2], A. Kadokura[2], M. Kozai[3], T. Kuwabara[4], M. Tokumaru[5], R. R. S. Mendonça[6], E. Echer[6], A. Dal Lago[6], M. Rockenbach[6], N. J. Schuch[6], J. V. Bageston[6], C. R. Braga[7], H. K. Al Jassar[8], M. M. Sharma[8], M. L. Duldig[9], J. E. Humble[9], P. Evenson[10], I. Sabbah[11]

[1] Physics Department, Shinshu University, Matsumoto, Japan, [2] National Institute of Polar Research, Tachikawa, Japan, [3]Institute of Space and Astronautical Science, Japan Aerospace Exploration Agency, Sagamihara, Japan, [4]Graduate School of Science, Chiba University, Chiba City, Japan, [5]Institute for Space-Earth Environmental Research, Nagoya University, Nagoya, Japan, [6]National Institute for Space Research, São José dos Campos, Brazil, [7]George Mason University, Fairfax, VA, USA, [8]Physics Department, Kuwait University, Kuwait City, Kuwait, [9]School of Natural Sciences, University of Tasmania, Hobart, Australia, [10]Bartol Research Institute, Department of Physics and Astronomy, University of Delaware, Newark, DE, USA, [11]Department of Applied Sciences, College of Technological Studies, Public Authority for Applied Education and Training, Shuwaikh, Kuwait.

PoS(ICRC2021)1265